Time-resolved terahertz spectroscopy of charge carrier dynamics in the chalcogenide glass $As_{30}Se_{30}Te_{40}$ [Invited]

Tianwu Wang,[1] Elena A. Romanova,[2] Nabil Abdel-Moneim,[3] David Furniss,[3] Anna Loth,[3] Zhuoqi Tang,[3] Angela Seddon,[3] Trevor Benson,[3] Andrei Lavrinenko,[1] and Peter Uhd Jepsen[1,*]

[1]*Department of Photonics Engineering (DTU Fotonik), Technical University of Denmark, DK-2800 Kgs. Lyngby, Denmark*
[2]*Saratov State University, Department of Physics, Astrakhanskaya 83, Saratov 410012, Russia*
[3]*Faculty of Engineering, University of Nottingham, University Park, Nottingham NG7 2RD, UK*
**Corresponding author: puje@fotonik.dtu.dk*

Received February 8, 2016; revised April 19, 2016; accepted April 19, 2016;
posted April 22, 2016 (Doc. ID 259125); published May 24, 2016

Broadband (1.6–18 THz) terahertz time-domain spectroscopy (THz-TDS) and time-resolved terahertz spectroscopy (TRTS) were performed on a 54 μm thick chalcogenide glass ($As_{30}Se_{30}Te_{40}$) sample with a two-color laser-induced air plasma THz system in transmission and reflection modes, respectively. Two absorption bands at 2–3 and 5–8 THz were observed. TRTS reveals an ultrafast relaxation process of the photoinduced carrier response, well described by a rate equation model with a finite concentration of mid-bandgap trap states for self-trapped excitons. The photoinduced conductivity can be well described by the Drude–Smith conductivity model with a carrier scattering time of 12–17 fs, and we observe significant carrier localization effects. A fast refractive index change was observed 100 fs before the conductivity reached its maximum, with 2 orders of magnitude larger amplitude than expected for the optically induced THz Kerr effect, indicating that free carriers are responsible for the transient index change.

OCIS codes: (300.6495) Spectroscopy, terahertz; (300.6530) Spectroscopy, ultrafast; (160.2750) Glass and other amorphous materials; (160.4330) Nonlinear optical materials; (160.5140) Photoconductive materials.
http://dx.doi.org/10.1364/PRJ.4.000A22

1. INTRODUCTION

Chalcogenide glasses exhibit several types of photoinduced phenomena, including photoinduced changes in local atom configuration, as has been investigated extensively [1–3]. High optical nonlinearity is a key factor for chalcogenide glasses to be useful for photonic devices; as for a given glass system, the nonlinearity of chalcogenide glasses increases as the optical bandgap energy decreases [3]. The optical bandgap energy depends on the composition, which decreases in the series Se → Te [4,5]. It is relevant to investigate the photoinduced charge carrier dynamics in highly nonlinear chalcogenide glasses. The first investigations of conductivity in chalcogenide glasses go back to the 1970s and 1980s [6–8]. Two theoretical models based on hopping between localized states have been proposed to explain the measured ac conductivity [3,6,7]. The conductivity in many chalcogenide glasses is governed by holes. However, in glasses with large concentrations of tellurium, the metallic character increases [4] but, to date, ac conductivity measurements in these glasses are limited to frequencies up to 10^7 Hz. However, in conductors with scattering times in the 10–100 fs range, such as in amorphous materials, the conductivity dynamics span an extremely broad frequency range, typically from the gigahertz to the terahertz (THz) range. Therefore, broadband, frequency-dependent THz conductivity measurements are required for a detailed understanding of the photoinduced charge carrier dynamics in chalcogenide glasses, as well as for extraction of fundamental carrier dynamics parameters, such as the mobility and scattering time.

Chalcogenide glasses have been characterized in the low THz region, where the amorphous, glassy structure leads to a universal dielectric function [9–11]. We have previously reported on the dielectric properties of the chalcogenide glasses As_2S_3 and GaLaS in a broader frequency range, revealing the cross-over frequency between universal absorption given by disorder and distinct absorption bands given by the specific material composition as narrow vibrational bands [12]. Together with the speed of sound in the material, this cross-over frequency determines a characteristic length scale of the local order in an amorphous material.

Here we report on the static dielectric properties and transient photoconductive properties of tellurium-doped arsenic selenide ($As_{30}Se_{30}Te_{40}$) in the 1–18 THz range (33–600 cm^{-1}). We find that the dielectric function is well described by that of two vibrational modes. The photoinduced conductivity can be described by a conductivity model that takes confinement of carriers into account, and the conductivity dynamics is well described by a standard model for carriers in disordered materials.

2. EXPERIMENTAL METHODS

The static and transient optical properties of the samples are characterized in the THz frequency range using THz time-domain spectroscopy (THz-TDS) [13,14]. The setup for static and transient THz spectroscopy is schematically illustrated in Fig. 1. Femtosecond laser pulses from a commercial amplified laser system (SpectraPhysics Spitfire Pro) with central wavelength 800 nm, pulse duration 35 fs, and pulse energy up to 3 mJ are used to drive the experimental setup.

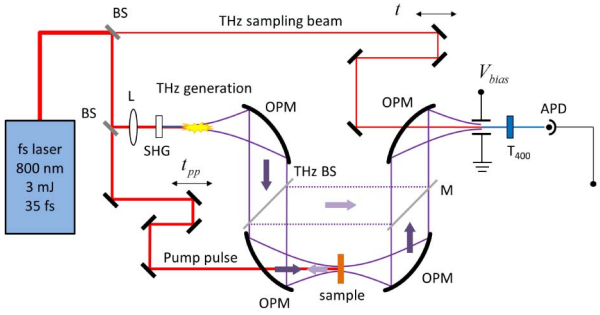

Fig. 1. Experimental setup for static and transient THz-TDS. For static spectroscopy, the pump pulse is blocked. The THz beam splitter (BS) together with mirror M are used in reflection mode.

Ultrabroadband THz pulses are generated by focusing the laser pulses with their second harmonics in air, thereby creating an extended air plasma. The nonlinear photocurrents in this plasma channel generate an intense, broadband THz transient [15–18], emitted in a conical shape in the forward direction from the focal region of the plasma [19,20]. The estimated peak field strength in the time domain incident on the sample is 50–100 kV/cm, and we have observed no indications of a nonlinear response from the sample. The THz pulses propagate through a standard system of off-axis paraboloidal mirrors (OPM), and are detected by air-biased coherent detection (ABCD) [21] with an avalanche photodiode (APD) for linear detection of the THz-induced second-harmonic of the THz sampling beam in the detection region [22].

In ABCD, two closely spaced electrodes enclose the focal region where both the THz beam after the final OPM and the 800 nm sampling beam are focused. The electrodes are biased with a kilovolt-level high voltage modulated at half the laser repetition rate (500 Hz). A lock-in amplifier phase locked to the 500 Hz modulated signal coherently picks up the second-harmonic of the 800 nm sampling beam with an intensity proportional to the instantaneous THz electric field strength. By scanning of the time delay, t, the complete waveform of the THz pulse can be recorded. For time-resolved THz spectroscopy (TRTS), an optical pump pulse as a specific pump–probe delay t_{pp} can be directed to the sample, and the optical properties at THz frequencies at that specific delay can then be recorded. All measurements can be performed in transmission or reflection. In reflection mode, a THz beam splitter (an undoped, high-resistivity silicon wafer) and a mirror are inserted in the THz beam path, as shown in Fig. 1, so that the THz waveform from the sample is recorded. The silicon beam splitter is simultaneously used to block the 800/400 nm pump light from the THz generation.

3. SAMPLE PREPARATION

For the glass synthesis, arsenic (7N, Furukawa Denshi Co. Ltd) and selenium (5N, Mateion) were prepurified by heating under vacuum (10^{-3} Pa) at 310°C and 270°C, respectively; the tellurium (5N, Cerac) was used as received. The glass precursors were each batched into a prepurified silica-glass ampoule, which was then evacuated and sealed. Glass melting was carried out with the following schedule. (i) The temperature was raised from room temperature to 250°C at 30°C per hour. (ii) Following a dwell at 250°C for 2 h, rocking of the furnace was started and the temperature increased to 800°C at a rate of 40°C per hour. (iii) The melting continued at 800°C, with rocking, for a further 12 h. (iv) The melt was then cooled from 800°C to 650°C at 40°C per hour while still rocking. (v) Finally, the rocking was then stopped and the melt held at 650°C for 4 h before quenching under a nitrogen gas jet as the ampoule was gradually withdrawn from the furnace. The glass rod produced was then annealed by heating at 138°C (the onset glass transition temperature, T_g, for this composition is 130 ± 5°C) for 2 h, followed by cooling to 65°C at 5 °C per hour and then from 65°C to room temperature at 20°C per hour. Circular disks of 10 mm diameter and 1.7 mm thick were cut (Leco, diamond wafer blade) from the annealed $As_{30}Se_{30}Te_{40}$ glass rod.

The glass disks used for the present work each underwent a generic optical sample preparation procedure before being pressed to form the thin sample measured. This involved polishing both sides of the disks using silicon carbide powder (400 grit and 1000 grit progressively; supplier Buehler) with silicone-based polishing oil (supplier Buehler) as the lubricant medium. Both sides were subsequently polished to a 1 μm finish using a Metaserv 2000 polishing wheel and progressively finer Metaserv diamond paste. The samples were then hot pressed under vacuum at ~25°C above the onset T_g between two tungsten carbide disks (each of 100 mm diameter, flatness 0.08 μm, and of surface finish 0.009 μm) and then annealed at T_g and allowed to cool with the press. The same tungsten carbide plates were used to further hot press one of the $As_{30}Se_{30}Te_{40}$ samples to form the ultrathin sample for the present measurements. This subsequent hot pressing was undertaken at ~28°C above T_g, followed by cooling with the press, and yielded a sample of thickness 54 μm.

4. COMPLEX REFRACTIVE INDEX OF $As_{30}Se_{30}Te_{40}$

The optical properties of the free-standing 54-μm-thick $As_{30}Se_{30}Te_{40}$ sample are measured in transmission THz-TDS. The THz time domain traces transmitting through sample and air are compared in Fig. 2. The absorption dip at 18.5 THz is caused by phonon overtone absorption in the silicon pump beam block. After transmission through the sample, the single-cycle THz pulse broadens somewhat in time due to the material dispersion. The oscillation near 2.5 ps is the first Fabry–Perot reflection inside the sample, which will cause

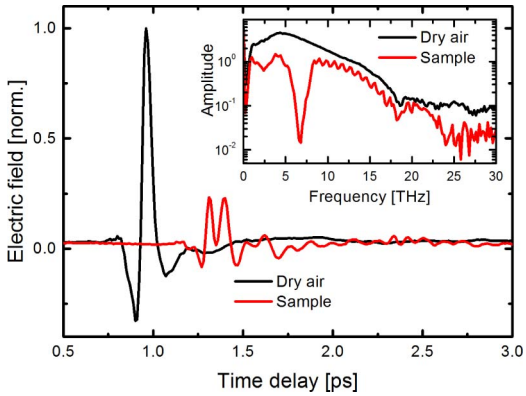

Fig. 2. THz time domain traces transmitting through a 54-μm-thick sample of $As_{30}Se_{30}Te_{40}$ and dry air. The inset shows the corresponding Fourier transformed spectra.

oscillations for the corresponding Fourier transformed spectrum, shown in the inset of Fig. 2.

The two dips in the spectrum are attributed to the corresponding two resonance modes of the sample. A specialized extraction algorithm that takes into account the reflection is used to calculate the optical parameters [13]. The extracted refractive index and absorption coefficient are shown in Fig. 3(a). The absorption band at 2–3 THz corresponds to different bond-bending vibrations [23], and the strong broadband at 5–8 THz is attributed to the antisymmetric As–Se–As stretching vibration $AsSe_3$ pyramidal units [4]. At high frequencies above 9 THz, the absorption coefficient levels off at a relatively low value of approximately 50 cm^{-1}. The permittivity can be directly calculated from the index of refraction and the absorption coefficient, and is shown in Fig. 3(b). Vibrational modes can typically be described by the Lorentz oscillator model. For two oscillator modes, we use the expression for the permittivity,

$$\varepsilon(\omega) = \varepsilon_\infty + \frac{A_1}{\omega_1^2 - \omega^2 - i\gamma_1\omega} + \frac{A_2}{\omega_2^2 - \omega^2 - i\gamma_2\omega}, \quad (1)$$

to extract the resonance frequencies, damping rates, and oscillator strengths for the two modes, as shown in Table 1.

A fit with a double-Lorentz model to the experimental data is shown together with the experimental data in Fig. 3. The complex refractive index of $As_{30}Se_{30}Te_{40}$ will be used for the TRTS.

5. TRTS

$As_{30}Se_{30}Te_{40}$ has a low electronic bandgap of 1.06 eV, defined as the spectral position where optical absorption exceeds

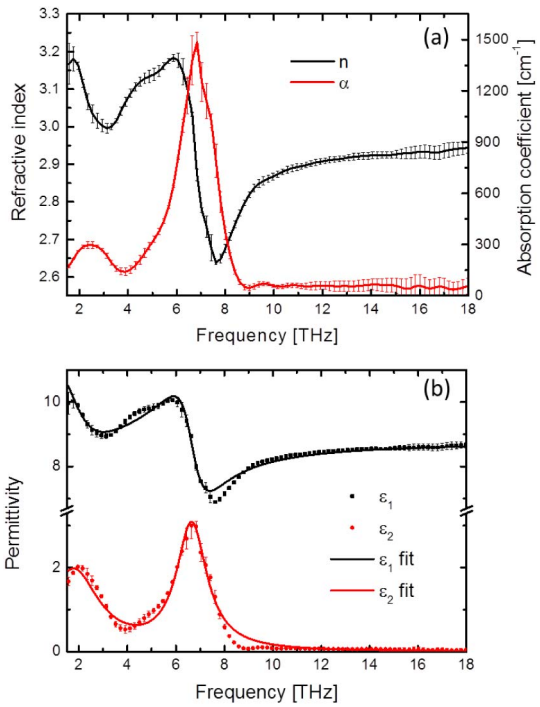

Fig. 3. (a) Refractive index and absorption coefficient and (b) the real and imaginary parts of the complex permittivity of $As_{30}Se_{30}Te_{40}$. The error bars indicate the standard deviation based on three individual measurements.

Table 1. Parameters for the Oscillator Model for $As_{30}Se_{30}Te_{40}$

Mode i	1	2
ω_i [rad/ps]	13.6 ± 0.22	42.05 ± 0.08
γ_i [rad/ps]	16.8 ± 1.2	9.6 ± 0.3
A_i [rad^2/ps^2]	403 ± 25	1205 ± 25
ε_∞	8.76 ± 0.015	–

10^3 cm^{-1}. As described above, here we photoexcite the sample with 800 nm (1.55 eV) pump pulses of 40 fs duration, and fluences in the range 0.3–0.8 mJ/cm^2. The photoconductivity is probed by the broadband THz pulse at normal incidence in reflection mode. In this mode, the temporal resolution is determined by the duration of the optical pump pulse [24,25]. For a given pump–probe time delay t_{pp}, the relative photoinduced change $\Delta\tilde{r}(\omega, t_{pp}) = (\tilde{E}_p(\omega, t_{pp}) - \tilde{E}_0(\omega))/\tilde{E}_0(\omega) = \Delta\tilde{E}(\omega, t_{pp})/\tilde{E}_0(\omega)$ of the reflected THz field is related to the photoconductivity $\tilde{\sigma}$ of the surface layer [24,26]:

$$\Delta\tilde{r}(\omega, t_{pp}) = \left(\frac{1 - \tilde{r}_0}{\tilde{r}_0}\right) \frac{Z_0 d\tilde{\sigma}(\omega, t_{pp})}{1 + n + Z_0 d\tilde{\sigma}(\omega, t_{pp})}, \quad (2)$$

where $\tilde{r}_0 = (1 - \tilde{n})/(1 + \tilde{n})$ is the (frequency-dependent) reflectivity of the unpumped sample with refractive index $\tilde{n}$ [Fig. 3(a)], $Z_0 = 377\,\Omega$ is the free-space impedance, and $d = 10$ μm is the thickness of the photoexcited layer. In the small-signal limit $\Delta\tilde{r} \ll 1$, Eq. (2) can be written as

$$\Delta\sigma(t_{pp}) = \Delta r \cdot \frac{n^2 - 1}{2Z_0 d}, \quad (3)$$

which relates the peak of the photoinduced reflectivity to the average photoconductivity. Figure 4 shows the temporal dynamics of the average photoconductivity at pump fluences of 0.32–0.82 mJ/cm^2. From these data we have found that single-photon absorption is dominant, with a slight tendency of saturation at the highest fluences.

At all the pump fluences, the relaxation process can be described by combined fast and slow decay processes. The kinetics of the conductivity decay can be described by the model illustrated in the inset of Fig. 4(a). The experimental data show the photoconductivity induced by the pump pulse, converted from the induced reflectivity change by using a scattering time of 18 fs (see below) and a thickness of the photoexcited layer of 10 μm. The peak reflectivity modulation is 2% at the highest excitation fluence. The model results represented by the solid lines are inspired by a similar model describing carrier kinetics in photoexcited NaCl [27]. Carriers are excited from the valence band (VB) to the conduction band (CB) by the pump pulse with intensity profile $I(t)$, and the electrons and holes subsequently thermalize (cool) to the respective band minimums with rate γ_{cool}. Electrons and holes are rapidly captured in a finite population of self-trapped exciton (STE) states, a mechanism known from other disordered semiconducting materials. We assume that holes are trapped at a significantly higher rate than the electrons [27], and that the trapping rate of the electrons is limited by the available number of trap sites. The model can then be described by a set of first-order rate equations:

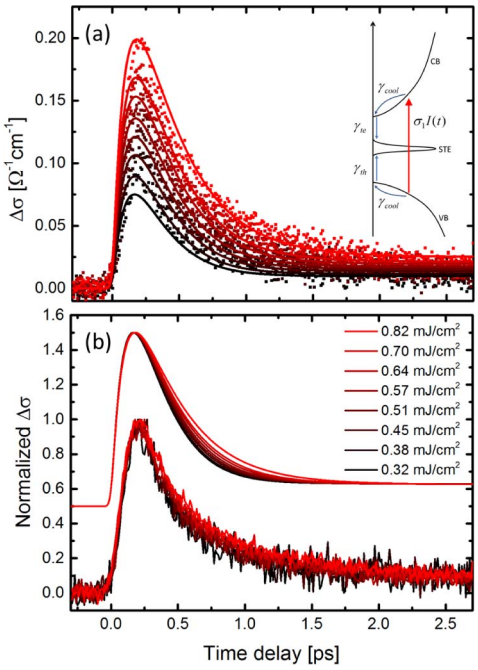

Fig. 4. (a) Differential reflectivity of the THz peak electric field as a function of pump–probe delay time for pump fluences of 0.32–0.82 mJ/cm^2. The symbols are experimental results, and the solid lines represent the decay kinetics model shown in the inset. (b) Normalized decay curves, which show that the kinetics slows down at increasing pump fluence.

$$\begin{aligned}
\dot{N}_{\mathrm{he}} &= \sigma_1 I(t) - \gamma_{\mathrm{cool}} N_{\mathrm{he}},\\
\dot{N}_e &= \gamma_{\mathrm{cool}} N_{\mathrm{he}} - \sigma_c N_e (N_{\mathrm{trap}} - N_{\mathrm{te}}),\\
\dot{N}_{\mathrm{te}} &= \sigma_c N_e (N_{\mathrm{trap}} - N_{\mathrm{te}}),\\
\dot{N}_{\mathrm{th}} &= \gamma_{\mathrm{th}} N_h,\\
\dot{N}_h &= \gamma_{\mathrm{cool}} N_{\mathrm{hh}} - \gamma_{\mathrm{th}} N_h,\\
\dot{N}_{\mathrm{hh}} &= \sigma_1 I(t) - \gamma_{\mathrm{cool}} N_{\mathrm{hh}},
\end{aligned} \tag{4}$$

where $N_{\mathrm{he}}, N_e, N_{\mathrm{te}}, N_{\mathrm{th}}, N_h, N_{\mathrm{hh}}$ are the concentrations of hot electrons, thermalized electrons, trapped electrons, trapped holes, thermalized holes, and hot holes, respectively, normalized with respect to a critical density $N_c = \omega^2 \varepsilon_0 m^*/e^2 = 9 \times 10^{20}$ cm^{-3} for an 800 nm pump wavelength. The single-photon absorption cross section $\sigma_1 = \alpha(h\nu)^{-1} N_c^{-1}$. The trapping cross section $\sigma_c = \sigma_{\mathrm{capture}} \cdot v \cdot N_c$ is based on estimates of the electron–hole capture cross section $\sigma_{\mathrm{capture}} = 8 \times 10^{-14}$ cm^2 as reported for NaCl [27–29], and the velocity of carriers is taken as the thermal velocity of the carriers at room temperature. We have used electron and hole cooling rates $\gamma_{\mathrm{cool}} = 6.7$ ps^{-1} (150 fs time constant) and an ultrafast hole trapping rate $\gamma_{\mathrm{th}} = 5$ ps^{-1} (200 fs time constant). Finally, the trap density was set to $N_{\mathrm{trap}} = 8.85 \times 10^{18}$ cm^{-3}. The photoconductivity is proportional to the product of the charge carrier concentration and mobility:

$$\Delta\sigma(t) \propto N_e(t)/m_e^* + N_{\mathrm{te}}(t)/m_{\mathrm{te}}^*. \tag{5}$$

The free carriers will have a Drude-like response, whereas the STE will have a bound-state response. However, the detailed parameters for the STE (resonance frequency, oscillator strength, damping) are difficult to estimate. The effective masses used here are $m_e^* = 0.5 m_0$ and $m_{\mathrm{te}}^* = 10 m_0$. With these considerations, the transient photoconductivity for the different excitation fluences can be modeled as shown in Fig. 4(a) (solid curves). The simulated curves have arbitrary absolute amplitude, and have been scaled so that the peak of the simulated photoconductivity at highest excitation density coincides with that of the corresponding experimental data. Figure 4(b) shows the same data in a normalized fashion, which allows a comparison between the observed trend in experiment that the dynamics slows down at higher excitation fluence, a trend that is reproduced by the model. This behavior is in contrast to the decay dynamics in NaCl [27], where a faster initial decay has been observed at higher multiphoton excitation fluence. Although our initial modeling of the decay dynamics of the carriers in $As_{30}Se_{30}Te_{40}$ at single-photon excitation offers a reasonable explanation of the process, there is clearly a need for further investigation of the processes to establish better estimates of the various parameters in the model.

To shed further light on the nature of the conductivity in $As_{30}Se_{30}Te_{40}$, we performed a full spectroscopic study of the temporal evolution of the frequency-dependent photoconductivity. This method, known as TRTS, is performed by recording the full temporal profile of the reflected THz field for a range of pump–probe delay times. The practical implementation of the measurements involves simultaneous recording of the pump and reference signals [30] and follows a standard data extraction scheme [13,24].

The temporal evolution of the photoinduced complex conductivity calculated from Eq. (2) is shown in Fig. 5. The THz waveforms were measured at 15 different pump–probe delay

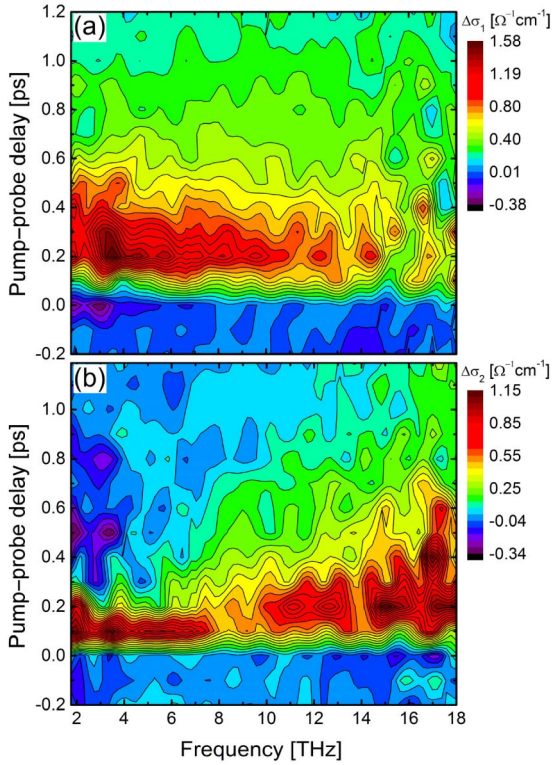

Fig. 5. 2D map of (a) the real part and (b) the imaginary part of the photoinduced ultrafast conductivity of $As_{30}Se_{30}Te_{40}$ at a pump fluence of 0.7 mJ/cm^2.

times with time interval of 100 fs. Similar to the results in Fig. 4, we observe a rapid increase and subsequent decay of the photoconductivity. As will be discussed in some more detail below, the real part of the conductivity has its maximum at a frequency higher than zero, indicative of some degree of carrier localization. Additionally, the rise of the imaginary part of the photoconductivity precedes that of the real part by approximately 100 fs. If the photoinduced conductivity change is converted to a refractive index change ($n = \sqrt{\varepsilon} = \sqrt{\varepsilon_\infty + i\sigma/\varepsilon_0\omega}$), as shown in Fig. 6, then the maximum refractive index change is +0.14, which is 100 times bigger than what could be expected from an optically induced Kerr effect [31]. The fast refractive index change comes 100 fs before the real conductivity reaches the maximum and decays within 100 fs, similar to the decay of the imaginary part of the photoconductivity.

The photoinduced complex conductivity at pump–probe delay $t_{pp} = 100$ fs is plotted in Fig. 7.

The real part of the conductivity is positive and decreases with decreasing frequency at low frequencies, and the imaginary part close to dc frequency becomes negative. There is a tendency that the real part of the photoconductivity peaks at a frequency higher than zero. Similar behavior has also been observed in a wide range of disordered nanoscale conductive materials, including semiconducting polymers [24] and silicon nanocrystalline films [25,32]. The Drude–Smith model, which phenomenologically includes carrier localization, describes the conductivity with an extension of the Drude model [24,33]:

$$\sigma(\omega) = \frac{\omega_p^2 \varepsilon_0 \tau}{1 - i\omega\tau}\left(1 + \frac{c}{1 - i\omega\tau}\right), \tag{6}$$

where ω_p is the plasma frequency, τ is the carrier scattering time, and c is the backscattering parameter, which describes carrier confinement in a phenomenological manner. For the $As_{30}Se_{30}Te_{40}$ chalcogenide glass, the localization of carriers is likely to be due to the amorphous structure of the glass matrix, with local regions of partial short-range order. Localization due to formation of STEs could also contribute to the observed localization. However, the simple, phenomenological model applied here does not offer a detailed description of the nature of the confinement.

A fit of Eq. (6) to the experimental data is shown as the solid curves in Fig. 7. The extracted scattering time is $\tau = 17.9$ fs and the backscattering parameter is $c = -0.52$. Considering a thermal velocity $v_{th} = \sqrt{3k_BT/m^*} = 1.65 \times 10^5$ m/s, with an effective mass $m^* = 0.5m_0$ and $T = 300$ K, the mean free path is $l_{mf} = v_{th}\tau = 2.9$ nm and the carrier mobility is estimated as $\mu = e\tau/m^* = 63$ cm^2/Vs.

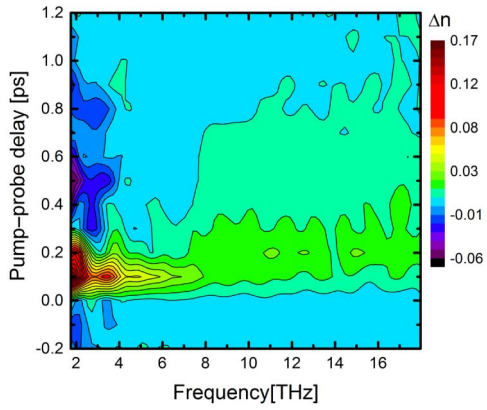

Fig. 6. 2D map of photoinduced refractive index change of $As_{30}Se_{30}Te_{40}$ in reflection measurement at pump fluence of 0.7 mJ/cm^2.

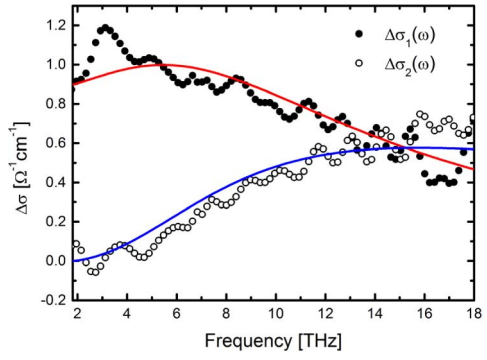

Fig. 7. Complex photoinduced conductivity of $As_{30}Se_{30}Te_{40}$ at pump fluence of 0.7 mJ/cm^2. The solid lines are the fits based on the Drude–Smith model.

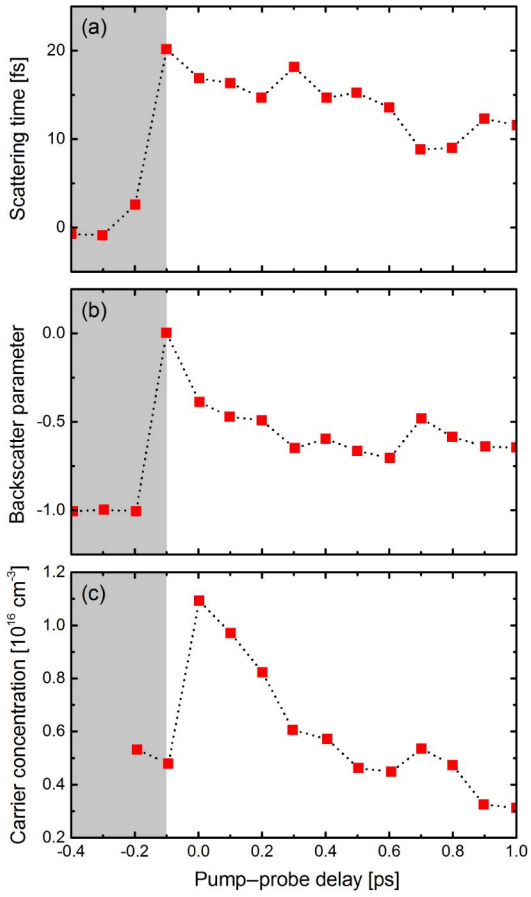

Fig. 8. Temporal development of the carrier dynamics parameters for $As_{30}Se_{30}Te_{40}$ extracted from the Drude–Smith model fits at different pump–probe delays. (a) Carrier scattering time τ, (b) backscattering parameter c, and (c) carrier density. The shaded areas indicate the time at which the probe pulse arrives before the pump pulse, with poorly defined fit parameters.

The fitting parameters extracted from Drude–Smith model [Eq. (6)] at different pump–probe delays are plotted in Fig. 8.

The scattering time slowly decreases from 18 to 12 fs; correspondingly, the mean free path decreases from 2.9 to 2.1 nm. The c parameter decreases significantly from −0.4 to −0.64. Thus, after injection, we see an indication that carriers become more localized within the first picosecond. The peak carrier density at probe delay $\tau_p = 0$ ps is 1.1×10^{16} cm^{-3}, which by comparison to the photon flux gives a pump photon flux gives a very low photon to carrier conversion efficiency of 0.09%. While a direct interpretation of the parameters extracted from the Drude–Smith fit is difficult, we conclude that the onset of localization is visible in the time-resolved photoconductivity spectra, which is consistent with the rate equation model developed to interpret to kinetics of the photoconductivity decay.

6. CONCLUSION

In summary, we have investigated the static dielectric properties and the transient photoconductive properties of the tellurium-rich semiconducting chalcogenide glass $As_{30}Se_{30}Te_{40}$. We have applied broadband transmission THz-TDS for linear characterization of the dielectric properties in the 1.6–18 THz range, and reflection TRTS for the characterization of the temporal and spectral dynamics of the photoinduced conductivity after excitation above the bandgap with femtosecond laser pulses at 800 nm. The kinetics of the conductivity is well described by a rate equation model that includes a finite density of trapping centers for STEs, and we find that the conductivity of these bound states must be included in the modeling of the response in order to find agreement with experiment.

The spectrally resolved conductivity dynamics was measured with 100 fs time resolution, allowing additional insight into the carrier dynamics. The transient conductivity spectra show localization of the carriers within 1 ps after photoexcitation, consistent with the assumptions of the simple kinetic model.

The presented model offers new values for certain critical parameters, such as the time constants of the trapping processes, the electron–phonon scattering time of the free carriers, and localization of the carriers. However, the good agreement between the presented model and the experimental data relies partially on specific values of certain critical parameters, such as the effective mass and capture rates, which are based on estimates from different material systems. It is therefore highly relevant to continue the exploration of the conductivity dynamics of this class of chalcogenide soft glasses, together with exploration of their nonlinear properties in the THz region.

ACKNOWLEDGMENT

T. W. and P. U. J. acknowledge financial support from the Danish Research Council for Independent Research (FNU Project THz-BREW).

REFERENCES

1. V. G. Ta'eed, N. J. Baker, L. Fu, K. Finsterbusch, M. R. E. Lamont, D. J. Moss, H. C. Nguyen, B. J. Eggleton, D. Y. Choi, S. Madden, and B. Luther-Davies, "Ultrafast all-optical chalcogenide glass photonic circuits," Opt. Express **15**, 9205–9221 (2007).
2. K. Petkov and P. J. S. Ewen, "Photoinduced changes in the linear and non-linear optical properties of chalcogenide glasses," J. Non-Cryst. Solids **249**, 150–159 (1999).
3. A. Zakery and S. R. Elliott, "Optical properties and applications of chalcogenide glasses: a review," J. Non-Cryst. Solids **330**, 1–12 (2003).
4. A. Zakery and S. R. Elliott, *Optical Nonlinearities in Chalcogenide Glasses and Their Applications*, Vol. **135** of Springer Series in Optical Sciences (Springer, 2007).
5. K. A. Aly, "Optical band gap and refractive index dispersion parameters of $As_xSe_{70}Te_{30-x}$ ($0 < x < 30$ at.%) amorphous films," Appl. Phys. A **99**, 913–919 (2010).
6. M. B. El-Den, N. B. Olsen, I. H. Pedersen, and P. Viscor, "DC and AC electrical transport in AsSeTe systems," J. Non-Cryst. Solids **92**, 20–30 (1987).
7. P. Viščor and N. B. Olsen, "Frequency and time response in relaxation time semiconductors," J. Non-Cryst. Solids **90**, 25–28 (1987).
8. R. A. Street, "Luminescence in amorphous semiconductors," Adv. Phys. **25**, 397–453 (1976).
9. E. P. J. Parrott, J. A. Zeitler, L. F. Gladden, S. N. Taraskin, and S. R. Elliott, "Extracting accurate optical parameters from glasses using terahertz time-domain spectroscopy," J. Non-Cryst. Solids **355**, 1824–1827 (2009).
10. S. N. Taraskin, S. I. Simdyankin, S. R. Elliott, J. R. Neilson, and T. Lo, "Universal features of terahertz absorption in disordered materials," Phys. Rev. Lett. **97**, 055504 (2006).
11. J. C. Dyre and T. B. Schroder, "Universality of ac conduction in disordered solids," Rev. Mod. Phys. **72**, 873–892 (2000).
12. M. Zalkovskij, C. Z. Bisgaard, A. Novitsky, R. Malureanu, D. Savastru, A. Popescu, P. U. Jepsen, and A. V. Lavrinenko, "Ultrabroadband terahertz spectroscopy of chalcogenide glasses," Appl. Phys. Lett. **100**, 031901 (2012).
13. P. U. Jepsen, D. G. Cooke, and M. Koch, "Terahertz spectroscopy and imaging–modern techniques and applications," Laser Photon. Rev. **5**, 124–166 (2011).
14. T. Wang, P. Klarskov, and P. U. Jepsen, "Ultrabroadband THz time-domain spectroscopy of a free-flowing water film," IEEE Trans. Terahertz Sci. Technol. **4**, 425–431 (2014).
15. D. J. Cook and R. M. Hochstrasser, "Intense terahertz pulses by four-wave rectification in air," Opt. Lett. **25**, 1210–1212 (2000).
16. M. Kress, T. Löffler, S. Eden, M. Thomson, and H. G. Roskos, "Terahertz-pulse generation by photoionization of air with laser pulses composed of both fundamental and second-harmonic waves," Opt. Lett. **29**, 1120–1122 (2004).
17. X. Xie, J. M. Dai, and X. C. Zhang, "Coherent control of THz wave generation in ambient air," Phys. Rev. Lett. **96**, 075005 (2006).
18. K. Y. Kim, A. J. Taylor, J. H. Glownia, and G. Rodriguez, "Coherent control of terahertz supercontinuum generation in ultrafast laser-gas interactions," Nat. Photonics **2**, 605–609 (2008).
19. Y. S. You, T. I. Oh, and K. Y. Kim, "Off-axis phase-matched terahertz emission from two-color laser-induced plasma filaments," Phys. Rev. Lett. **109**, 183902 (2012).
20. P. Klarskov, A. C. Strikwerda, K. Iwaszczuk, and P. U. Jepsen, "Experimental three-dimensional beam profiling and modeling of a terahertz beam generated from a two-color air plasma," New J. Phys. **15**, 075012 (2013).
21. J. Dai, X. Xie, and X. C. Zhang, "Detection of broadband terahertz waves with a laser-induced plasma in gases," Phys. Rev. Lett. **97**, 103903 (2006).
22. T. Wang, K. Iwaszczuk, E. A. Wrisberg, E. V. Denning, and P. U. Jepsen, "Linearity of air-biased coherent detection for terahertz time-domain spectroscopy," J. Infrared Millim. Terahertz Waves **37**, 592–604 (2016).
23. J.-L. Adam and X. Zhang, *Chalcogenide Glasses: Preparation, Properties and Applications* (Woodhead, 2013).
24. D. G. Cooke, F. C. Krebs, and P. U. Jepsen, "Direct observation of sub-100 fs mobile charge generation in a polymer-fullerene film," Phys. Rev. Lett. **108**, 056603 (2012).
25. D. G. Cooke, A. Meldrum, and P. U. Jepsen, "Ultrabroadband terahertz conductivity of Si nanocrystal films," Appl. Phys. Lett. **101**, 211107 (2012).
26. D. A. Valverde-Chavez, C. S. Ponseca, C. C. Stoumpos, A. Yartsev, M. G. Kanatzidis, V. Sundstrom, and D. G. Cooke,

"Intrinsic femtosecond charge generation dynamics in single crystal $CH_3NH_3PbI_3$," Energy Environ. Sci. **8**, 3700–3707 (2015).
27. P. Martin, S. Guizard, P. Daguzan, G. Petite, P. D'Oliveira, P. Meynadier, and M. Perdrix, "Subpicosecond study of carrier trapping dynamics in wide-band-gap crystals," Phys. Rev. B **55**, 5799–5810 (1997).
28. R. T. Williams, J. N. Bradford, and W. L. Faust, "Short-pulse optical studies of exciton relaxation and F-center formation in NaCl, KCl, and NaBr," Phys. Rev. B **18**, 7038–7057 (1978).
29. S. C. Jones, A. H. Fischer, P. Braunlich, and P. Kelly, "Prebreakdown energy absorption from intense laser pulses at 532 nm in NaCl," Phys. Rev. B **37**, 755–770 (1988).
30. K. Iwaszczuk, D. G. Cooke, M. Fujiwara, H. Hashimoto, and P. U. Jepsen, "Simultaneous reference and differential waveform acquisition in time-resolved terahertz spectroscopy," Opt. Express **17**, 21969–21976 (2009).
31. M. Zalkovskij, A. C. Strikwerda, K. Iwaszczuk, A. Popescu, D. Savastru, R. Malureanu, A. V. Lavrinenko, and P. U. Jepsen, "Terahertz-induced Kerr effect in amorphous chalcogenide glasses," Appl. Phys. Lett. **103**, 221102 (2013).
32. D. G. Cooke, A. N. MacDonald, A. Hryciw, J. Wang, Q. Li, A. Meldrum, and F. A. Hegmann, "Transient terahertz conductivity in photoexcited silicon nanocrystal films," Phys. Rev. B **73**, 193311 (2006).
33. N. V. Smith, "Classical generalization of the Drude formula for the optical conductivity," Phys. Rev. B **64**, 155106 (2001).